crystals

MDPI

Article

Director Fluctuations in Two-Dimensional Liquid Crystal Disclinations

Olaf Stenull and Tom C. Lubensky *

Department of Physics and Astronomy, University of Pennsylvania, Philadelphia, PA 19104, USA; olaf.stenull@comcast.net

* Correspondence: tom@sas.upenn.edu

Abstract: We present analytical calculations of the energies and eigenfunctions of all normal modes of excitation of charge +1 two-dimensional splay (bend) disclinations confined to an annular region with inner radius R_1 and outer radius R_2 and with perpendicular (tangential) boundary conditions on the region's inner and outer perimeters. Defects such as these appear in islands in smectic-C films and can in principle be created in bolaamphiphilic nematic films. Under perpendicular boundary conditions on the two surfaces and when the ratio $\beta = K_s/K_b$ of the splay to bend 2D Frank constants is less than one, the splay configuration is stable for all values $\mu = R_2/R_1$. When $\beta > 1$, the splay configuration is stable only for μ less than a critical value $\mu_c(\beta)$, becoming unstable to a "spiral" mixed splay-bend configuration for $\mu > \mu_c$. The same behavior occurs in trapped bend defects with tangential boundary conditions but with K_s and K_b interchanged. By calculating free energies, we verify that the transition from a splay or bend configuration to a mixed one is continuous. We discuss the differences between our calculations that yield expressions for experimentally observable excitation energies and other calculations that produce the same critical points and spiral configurations as ours but not the same excitation energies. We also calculate measurable correlation functions and associated decay times of angular fluctuations.

Keywords: liquid crystals; thin films; disclination defects

Citation: Stenull, O.; Lubensky, T.C. Director Fluctuations in Two-Dimensional Liquid Crystal Disclinations. *Crystals* **2022**, *12*, 1. https://doi.org/10.3390/cryst12010001

Academic Editor: Charles Rosenblatt

Received: 18 November 2021
Accepted: 17 December 2021
Published: 21 December 2021

1. Introduction

We are honored to submit this paper in celebration of Noel Clark's 80th birthday. Noel is a giant of our community. He has made major contributions to almost every aspect of liquid-crystal (LC) science with contributions to soft-matter in general as a bonus: fundamental and applied, light and X-ray scattering, displays and other applications spawning at least three startup companies, ferroelectric LCs (most recently a true three-dimensional (3D) fluid version [1]), ferronematics, banana LC's, defects in LCs, LCs in random environments, lyotropic lamellar phases, DNA LC's along with speculations about the origin of life, de Vries smectics, and the list goes on. This paper is a small contribution to one of the fields, freely-suspended or free-standing LC films [2,3], in which Noel has been a leading figure from the beginning—as coauthor of the first paper on the subject [4] and in over 25 papers (some of which are cited here [5–22]) that followed. These few-layer-thick smectic-C (Sm-C) films [4] have provided, and the more recently discovered bolaamphiphilic nematic films [1,23] have the potential to provide, fertile ground for studying topological defects in liquid crystals [24–28] (LCs). Viewed under a microscope [4–9,11], these films give striking visual proof of the existence of point disclinations and their varied properties.

It is well established that thermal fluctuations lead to a spontaneous motion of these point disclinations akin to the Brownian motion of a particle [11,29,30]. We have found only two publications [31,32] that directly calculate fluctuation energies, not of simple splay or bend defects as shown in Figure 1, but of more complex spiral structures of Figure 2b displaying both splay and bend. These publications use a different parametrization than

ours that produces excitation energies that are positive throughout stable regions and that correctly identify the phase boundaries in Figure 3. These energies, however, unlike those we calculate, do not correspond to those that would be measured in an experiment as will be discussed in more detail in Section 6.

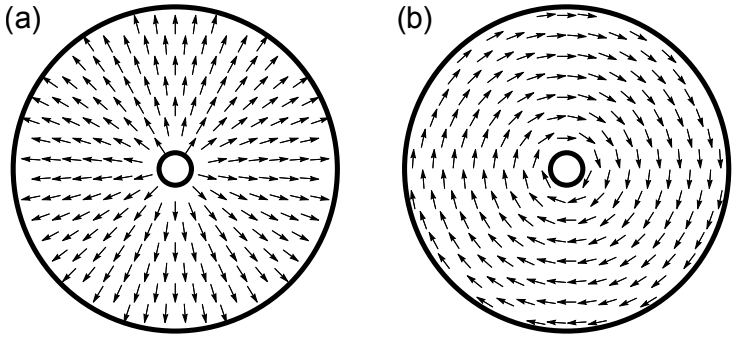

Figure 1. Sketches of in-plane **c**-director fields in annular traps with concentric outer and inner bounding circles with (**a**) perpendicular and (**b**) tangential boundary conditions.

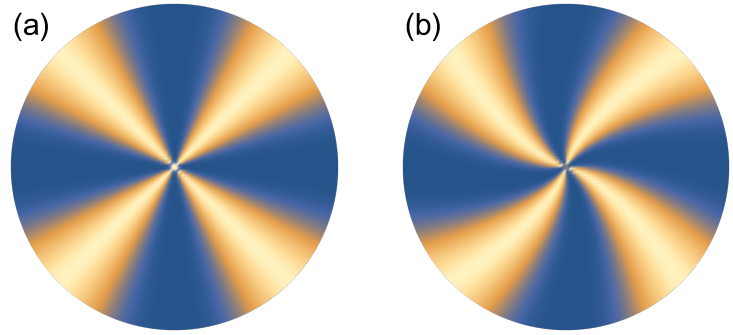

Figure 2. Computer generated images of (**a**) splay or bend defects and (**b**) spiral defects under crossed polarizers. The twisting or spiral structure is produced by a combination of splay and bend. The spiral structure was calculated with $\beta = 1.5$ and $\mu = 800$ corresponding to the orange curve in Figure 9.

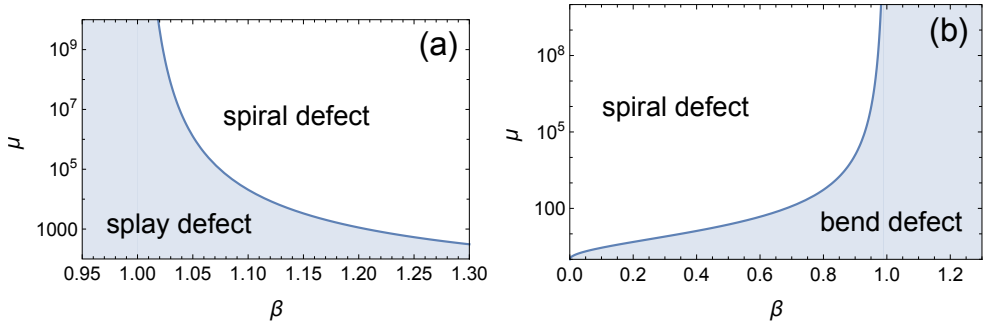

Figure 3. Phase diagrams for an annulus with (**a**) tangential and (**b**) perpendicular BCs. The dividing line between the two defect types is $\mu_c^{\mathrm{S}}(\beta)$ in (**a**) and $\mu_c^{\mathrm{B}}(\beta)$ in (**b**). In (**a**), the bend (spiral) defect is stable, and in (**b**), the splay (spiral) defect is stable in the shaded (unshaded) areas.

In smectic-C films, the nematic director **n** tilts relative to the local normal to smectic layers creating a component parallel to these layers that, when normalized to unit magnitude defines the **c**-director, $\mathbf{c}(\mathbf{r})$ that is a function of its spatial position **r**. Both splay and bend defects Figure 1, and even more complex twisting structures [16,32–34], are common in circular islands with extra smectic layers in freely-suspended Sm*C* films. Bend (splay) defects in **c** generally occur in systems in which the 2D Frank constant, K_b, for bend (units of energy) is less (greater) than the 2D splay constant K_s. The former condition is more common in nonpolar Sm*C* phases and the latter in ferroelectric SmC^* phases [33–35],

in which $K_b > K_s$ is a result of renormalization of K_b through couplings to the electric polarization [5,36]. Charge $S = +1$ defects also arise in films of anticlinic smectic phases (Sm-C_A) [37] and should, in principle, arise in bolaamphiphilic nematic films [23]. Core regions where Sm-C or nematic order vanishes can act as the inner circle of an annular island as can nematic or cholesteric (for chiral Sm-C^*) droplets [34] or even smoke particles [32]. To simplify our calculations, we will assume, following common practice [3], that the core region is a circle of radius R_1 the same boundary condition (BC) as the outer circle with radius R_2, i.e., perpendicular for splay and tangential for bend defects. In addition, we assume that the BCs do not change when $\mathbf{c}(\mathbf{r})$ is rotated through an angle of π about an inplane axis through $\mathbf{r}$. We also fix the inner circle to be at the center of the outer circle, thus ignoring diffusive motion of the inner core.

2. Results

We investigate the fluctuations of the inplane **c**-director field in an annular region, which we will refer to as a trap, of inner radius R_1 and outer radius R_2 holding a splay, bend, or mixed splay bend charge $S = +1$ disclination defect at its center. The properties of these defects, particularly their stability, depend on two the ratios:

$$\mu = \frac{R_2}{R_1} \qquad \text{and} \qquad \beta = \frac{K_s}{K_b}\,. \tag{1}$$

We begin with systems with perpendicular BCs. If $\beta < 1$, the energy (ignoring BCs), $\pi K_s \ln \mu$, of a pure splay defect is less than that, $\pi K_b \ln \mu$, of a pure bend defect. With these BCs, the splay defect is the stable, lowest-energy configuration for an annulus of any μ. On the other hand, if $\beta > 1$, the pure bend defect (again ignoring BCs) has lower energy than the pure splay defect. In this case, the enforced perpendicular alignment at boundaries stabilizes the splay state at small $\beta - 1$ because of the high energy cost of rotation from the pure splay state in the confined geometry defined by μ. As μ increases, however, there is more room for the rotation to occur, and at a critical value $\mu_c^S(\beta)$, the splay defect becomes unstable to the formation of a state, which we will refer to as the spiral state, with mixed splay and bend, as shown in Figure 3a. Alternatively, at fixed μ, the splay state is stable with respect to the spiral state for all β less than a critical value $\beta_c^S(\mu)$. A similar scenario occurs when the BCs are tangential. The pure bend defect is stable with respect to the spiral state for all β greater than a critical value $\beta_c^S(\mu)$ as shown in Figure 3b. Experiments reported in Ref. [35] display exactly the scenario just discussed: Islands with $K_b < K_s$ subjected to tangential boundary conditions adopt the bend defect geometry for all μ. Small area islands of polar SmC^* with $K_b > K_s$ and tangential boundary conditions adopt the pure bend configuration even though the bulk energy prefers the pure splay configuration. Upon increasing the area, the system undergoes a transition, when μ exceeds a critical value μ_c, to a spiral state. The value of μ_c decreases with decreasing K_b/K_s as we find. Approximate numerical calculations in Ref. [35] of the **c**-director fit the experiments very well. It should be noted that these calculations, like ours, model the system as an annulus with tangential boundary conditions at both interior boundaries. In what follows, we will often not display the superscripts S and B indicating splay and bend.

The energy of the lowest-energy normal mode (the critical mode) determines the stability of the splay state: if it is positive, the state is at least metastable; if it is negative, the state is unstable. The energy densities of normal modes are all expressed as $\varepsilon = K_b(\kappa/R_2)^2$ where κ is a unitless "wavenumber". When $\beta > 1$ and $\mu < \mu_c$, κ is real, and both κ and ε are positive, approaching zero at μ_c. When $\mu > \mu_c$, $\kappa = i\kappa'$ is imaginary, ε is negative, and both κ' and $|\varepsilon|$ rise from zero at μ_c. Figure 4 plots κ for the three lowest-energy modes as a function of μ. These results are repeated, but with K_s and K_b interchanged, for trapped bend defects subjected to tangential BCs. Figure 3 shows the phase diagrams for the traps with tangential and with perpendicular BCs.

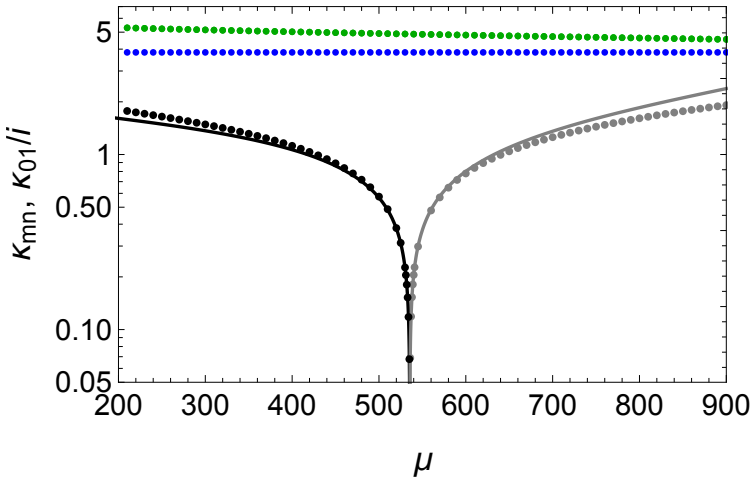

Figure 4. Wavenumbers κ_{mn} as a function of μ for our sample configurations with imaginary ν_0 and $\mu_c \approx 535$. The dots are obtained by numerical calculation of the zeros κ_{01} (black), κ_{02} (gray) and κ_{11} (blue) of the full function Z_{ν_m}. The black line stems from our approximate analytical solution for κ_{01} as given in Equation (20). Note the excellent agreement between the black dots and the black line for μ close to μ_c. Also note the steep rise of the κ_{01} near μ_c.

The two-dimensional ($2D$) scenario presented here follows closely the $3D$ scenario [38] for a radial hedgehog defect trapped in a spherical nematic emulsion droplet with a small spherical droplet at its center. The agreement between theory and experiment in the $3D$ case [39] is extremely good. In particular, because fluctuations diminish and become difficult to measure as the energies of the lowest-energy excitations increase, fluctuations in droplets with μ near μ_c are large and visible, whereas fluctuations in droplets with μ distant from μ_c are small and barely visible. The result is that only droplets with μ less than but close to μ_c exhibit observable fluctuations. Our prediction is that the same phenomenon should occur under appropriate conditions in $2D$.

This is a theoretical paper that provides a full analysis of fluctuations in trapped defects. In Section 3, we obtain analytic expressions for the complete eigenvalue spectrum and associated wavefunctions (Figure 5) of both splay and bend defects with perpendicular or tangential BCs at inner and outer circular boundaries. The results are a little unusual. The wavefunctions are Bessel functions of irrational or rational order, and the particular one associated with the critical soft mode is of imaginary order with either irrational or rational magnitude. In Section 4, we calculate the director correlation functions that might be measured in optical experiments. In Section 5, using an alternative parametrization in terms of $x = \ln r/R_1$ used in previous publications [31,32,34], we calculate the function $f(\mathbf{r})$ in the splay-defect system with for $\mu > \mu_c$ and show that there is a transition to lower-energy spiral state in systems with the soft mode. In Section 6, we campare results obtained by our procedure with those of the alternative parametrization that correctly calculates stable or metastable configurations, but provides normal-mode energies that are not part of the experimental fluctuation spectra. In the final Discussion section (Section 7), we review our results and speculate about future directions.

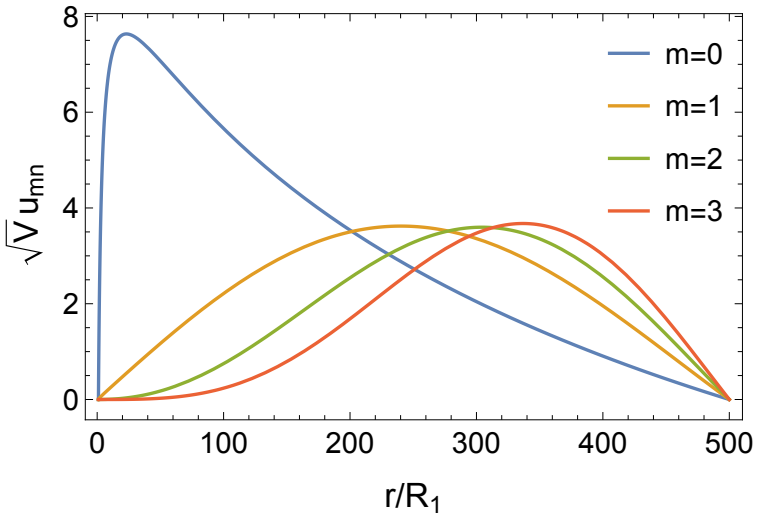

Figure 5. The radial eigenfunctions $u_{mn}(r)$, where m and n are, respectively, the standard integer azimuthal and radial quantum numbers for polar coordinates, for a system with the imaginary value of ν_0 used in Figure 6c. All plots are for $n = 1$, the lowest permitted value for n. On the ordinate, we included a factor $\sqrt{V}$, where $V = \pi R_2^2$ is the total area enclosed by the outer circle of the trap so that the plotted eigenfunctions are dimensionless.

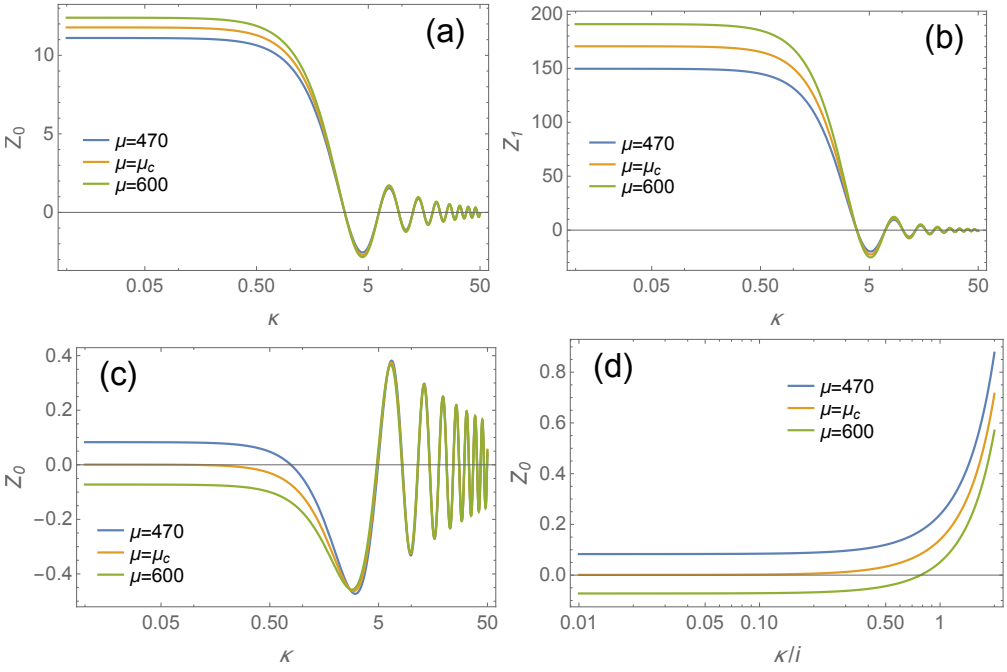

Figure 6. The functions $Z_0 \equiv Z_{\nu_0}$ as a function of κ for $\mu < \mu_c$, $\mu = \mu_c$ and $\mu > \mu_c$: (**a**) Z_0 for $\beta = 0.8 < 1$, (**b**) Z_1 for $\beta = 1.25 > 1$; (**c**) Z_0 for $\beta = 1.25$, and (**d**) $Z_0(\kappa)$ as a function of $\kappa' = \kappa/i$ for $\mu > \mu_c$. The rapid oscillations are a consequence of the logarithmic scale. Note that there are no zeros at small κ for (**a**,**b**) indicating large values of ε both for cases with $\beta < 1$ and for modes with $m = 1$ (and greater). In addition, the positions of the zeros in (**a**,**b**) are fairly insensitive to the value of μ and to the critical point. In (**c**), there is a zero in the top curve ($\mu < \mu_c$) that vanishes at μ_c and ceases to exist for $\mu > \mu_c$. In (**d**), there is a zero in bottom curve ($\mu > \mu_c$) that vanishes at μ_c and then disappears when $\mu < \mu_c$. Z_0 has an infinity of larger-value zeros in (**c**), whereas in (**d**), it has only one zero when $\mu \geq \mu_c$.

3. Theoretical Preliminaries

In 2D, there is no twist deformation, and the Frank elastic energy of a Sm*C* film is

$$F = \frac{1}{2}\int d^2r\Big\{K_s(\nabla\cdot\mathbf{c})^2 + K_b(\nabla\times\mathbf{c})^2\Big\}\,. \tag{2}$$

Here, K_s and K_b are the effective $2D$ Frank elastic constants for splay and bend, respectively. They depend on the original $3D$ Frank constants of the LC, the film thickness, and the tilt angle θ and have the units of energy.

3.1. Splay and Bend Disclinations

Because of the rotational symmetry of the boundaries of our droplets, it is useful to employ $2D$ polar coordinates where, as usual, r is the radius, ϕ the polar angle, and $\hat{e}_r$ and $\hat{e}_\phi$ are the corresponding basis vectors. Perpendicular BCs favor a $+1$ splay defect in which the **c**-director adopts the homogeneous, radial configuration $\mathbf{c} = \hat{e}_r$: tangential BCs favor a $+1$ bend defect with a circular configuration with $\mathbf{c} = \hat{e}_\phi$. Each of the two configurations and deviations from them can be parameterized by a scalar angle field (f or g):

$$\mathbf{c} = \cos f\,\hat{e}_r + \sin f\,\hat{e}_\phi \approx \left(1-\frac{1}{2}f^2\right)\hat{e}_r + f\hat{e}_\phi \qquad \text{splay,} \tag{3a}$$

$$\mathbf{c} = \sin g\,\hat{e}_r + \cos g\,\hat{e}_\phi \approx g\hat{e}_r + \left(1-\frac{1}{2}g^2\right)\hat{e}_\phi \qquad \text{bend,} \tag{3b}$$

where f and g are functions depending on $\vec{r} = (r,\phi)$.

The Frank energy for the splay defect expressed in terms of f is then [32]

$$\begin{aligned} F = \frac{1}{2}K\int\frac{d^2r}{r^2}\{&[1-\sigma\cos(2f)] + [1+\sigma\cos(2f)](r\partial_r f)^2 + 2\sigma\sin(2f)r\partial_r f \\ &+ (1-\sigma\cos 2f)(\partial_\phi f)^2 + 2(1-\sigma)\sin 2f\, r\,\partial_r f\,\partial_\phi f\}\,, \end{aligned} \tag{4}$$

where $K = (K_s+K_b)/2$ and $\sigma = (K_b-K_s)/(2K)$. The energy for a bend defect is identical to the above with K_s and K_b interchanged, or equivalently replacing σ by $-\sigma$. After expansion to harmonic order in f and some algebra, we can recast the Frank energy (relative to the equilibrium energy $\pi K_s\ln(R_2/R_1)$) as

$$F_h = \frac{1}{2}\int_{R_1}^{R_2} drr\int_0^{2\pi} d\phi\Big\{(K_b-K_s)\frac{1}{r^2}f^2 + K_s\frac{1}{r^2}(\partial_\phi f)^2 + K_b(\partial_r f)^2\Big\}. \tag{5}$$

3.2. Eigenvalue Problem

Next, we determine the eigenvalues and eigenfunctions of the Frank elastic energy in the harmonic limit as stated in Equation (5). Then, we expand the latter in terms of these eigenvalues and eigenfunctions which will allow us to calculate measurable quantities such as director correlation functions.

The eigensystem of F is determined by the characteristic equation

$$\frac{\delta F_h}{\delta f(\mathbf{r})} = \frac{1}{r^2}\Big\{(K_b-K_s) - K_s\partial_\phi^2 - K_b(r^2\partial_r^2 + r\partial_r)\Big\}f = \varepsilon\, f, \tag{6}$$

where ε is an eigenenergy density and where we used

$$\frac{\delta f(\mathbf{r})}{\delta f(\mathbf{r}')} = \delta(\mathbf{r}-\mathbf{r}') = \frac{1}{r}\delta(r-r')\delta(\phi-\phi')\,. \tag{7}$$

with $\mathbf{r} = r\hat{e}_r(\phi)$. Note the factors of r^{-2} on the first two terms but not on the ε term. This is a reflection of the $2D$ nature of the problem. We will return to this observation in Section 6.

To solve Equation (6), we note that the dependence of the polar angle is contained entirely in one term of the sum. This motivates a product ansatz of the form

$$f(r,\phi) = Au(r)\Phi(\phi)\,, \tag{8}$$

where for normalization purposes we choose $u(r)$ to have units of inverse length, A to have units of length, and $\Phi(\phi)$ to be unitless. Because f must be 2π-periodic in ϕ, we immediately deduce that

$$\Phi(\phi) = e^{im\phi}\,, \tag{9}$$

with integer m. After substitution of Equations (8) and (9) into Equation (6), the characteristic equation (after multiplying by r^2) becomes

$$\left[r^2\partial_r^2 + r\partial_r + k^2r^2 - \nu_m^2\right]u_m(r) = 0\,, \tag{10}$$

where

$$k = \sqrt{\frac{\varepsilon}{K_b}} \tag{11}$$

and

$$\nu_m = \sqrt{1 + (m^2-1)\frac{K_s}{K_b}}\,. \tag{12}$$

The ν_m parameters will take on an important role shortly as the indices of Bessel functions that are the main building blocks of our solution. They are in general irrational numbers that are all real for $m \geq 1$ so long as the elastic constants are positive, which we assume to be true. ν_0 is real when $K_s < K_b$, i.e., when the pure splay defect is favored over the pure bend defect, and it is imaginary when $K_b < K_s$ and the bend defect is favored. Whether ν_0 is real or imaginary has important qualitative consequences that we will discuss shortly. Equation (10) is the well-known Bessel differential equation whose solutions are linear combinations of Bessel functions of the first and second kind, $J_\nu(kr)$ and $Y_\nu(kr)$, respectively. We seek solutions that vanish at $r = R_1$ and $r = R_2$. The first condition is satisfied for any ν, k, and r by the linear combination,

$$Z_\nu(kr) = Y_\nu(kr)J_\nu(kR_1) - J_\nu(kr)Y_\nu(kR_1)\,. \tag{13}$$

The second condition is met when $\kappa_{mn} = k_{mn}R_2$ is the nth zero of $Z_{\nu_m}(kR_2)$:

$$Z_{\nu_m}(\kappa) = Y_{\nu_m}(\kappa)J_{\nu_m}(\kappa/\mu) - J_{\nu_m}(\kappa/\mu)Y_{\nu_m}(\kappa/\mu) = 0\,, \tag{14}$$

where

$$\kappa = kR_2\,, \tag{15}$$

and where n sequentially specifies the zeros with increasing values of κ.

The solutions κ_{mn} determine the energy of the modes mn:

$$\varepsilon_{mn} = K_b\left(\frac{\kappa_{mn}}{R_2}\right)^2. \tag{16}$$

When $m \geq 1$, all ν_m are real, and both $J_{\nu_m}(\kappa)$ and $Y_{\nu_m}(\kappa)$ and, consequently, $Z_{\nu_m}(\kappa)$ oscillates out to infinity and, therefore, $Z_{\nu_m}(\kappa)$ has an infinite number of zeros for each $m > 1$ (See Figure 6a,b). When $m = 0$, ν_0 is real when $K_s < K_b$ and imaginary when $K_b < K_s$. In the former case, the splay configuration has lower energy than that of the bend state in an infinite sample, and there is no instability (signaled by a vanishing mode) toward a state with bend and splay. In the latter case, shown in Figure 6c, the splay state has higher

energy than the pure bend state at $\mu \to \infty$ but lower energy imposed by the splay-favoring perpendicular BCs at sufficiently small μ. The value of $Z_{\nu_0}(0)$ depends on μ: it is positive for $\mu < \mu_c$, zero at $\mu = \mu_c$, and negative at $\mu > \mu_c$. When $\mu < \mu_c$, there is a zero in the function that approaches zero as $Z_{\nu_0}(\kappa)$ approaches 0 with κ. When $\mu > \mu_c$, the latter zero no longer exists. Thus, it appears the we have lost a solution altogether and that the curve of κ versus μ in Figure 4 simply stops. But, it turns out we missed a solution that occurs when $\kappa = i\kappa'$, where κ', is real as shown in Figure 6d. This solution, κ'_{01}, exists when ν_0 is imaginary and $\mu > \mu_c$; it disappears at $\mu = \mu_c$ and does not exist for $\mu < \mu_c$. Because κ is imaginary for this solution, the energy ϵ_{01} is negative, indicating that the radial hedgehog is unstable for all $\mu > \mu_c$, a result that should be expected because when μ becomes large, BCs become less important and the bend defect should win out when $K_b < K_s$.

The value of μ_c and the behavior of κ near μ_c is easily determined by expanding $Z_{\nu_0}(\kappa)$ to second order in κ

$$Z_{\nu_0}(\kappa) = \frac{\mu^{\nu_0} - \mu^{-\nu_0}}{\pi\nu_0}\left(1 - \lambda^2(\mu)\kappa^2 + \mathcal{O}\kappa^4\right). \tag{17}$$

An expression for λ will be given in Equation (20). For the moment we are interested in $Z_{\nu_0}(0)$. As Figure 6b shows, the zero of $Z_{\nu_0}(\kappa)$ that exists for $\mu < \mu_c$ vanishes when $Z_{\nu_0}(0)$ reaches zero, causing, as shown in Figure 6c, κ_{01} and ε_{01} to vanish. Thus, the critical point at which the radial defect becomes marginally unstable occurs at $Z_{\nu_0}(0) = 0$, or when

$$\mu = \mu_c(\beta) = \exp\left(\frac{i\pi}{\nu_0(\beta)}\right) \qquad \text{or equivalently} \qquad \beta(\mu) = \beta_c(\mu) = 1 + \left(\frac{\pi}{\ln\mu}\right)^2. \tag{18}$$

Note that because μ_c must be real, it only exists for values of the Frank constants for which ν_0 is imaginary (We ignore the hypothetical case that ν_0 could be exactly the inverse of a positive even integer). In our sample configuration with $\beta = 1.25$ and imaginary ν_0,

$$\mu_c = e^{2\pi} \approx 535.492\,. \tag{19}$$

What happens physically when μ approaches and crosses its critical value? To shed light on this question, it is instructive to see how the wavenumbers change near μ_c. For μ just below μ_c, κ_{01} is small, and we can obtain an approximate solution for it by calculating κ^2 by setting Equation (17) truncated to quadratic order equal to zero. The result is

$$\kappa_{01}^2(\mu) = \lambda^{-2}(\mu) = \frac{4\mu^2\left(1-\nu_0^2\right)\left(1-\mu^{2\nu_0}\right)}{(\mu^2+1)(1-\mu^{2\nu_0}) + \nu_0(\mu^2-1)(1+\mu^{2\nu_0})}\,. \tag{20}$$

Figure 4 shows a plot of κ_{01} vs. μ, i.e., a plot of the square root of this result along with with points calculated by the full Z_ν function.

Equation (20) encapsulates the behavior of κ near $\mu = \mu_c$ for both $\mu < \mu_c$ and $\mu > \mu_c$. From Equation (18), $\mu_c^{2\nu_0} = e^{2\pi i} = 1$ so that $\kappa_{01}(\mu_c)$ is zero as required. To determine $\kappa_{01}(\mu)$ for μ near μ_c, we expand μ to linear order in $\mu - \mu_c$. The result is $\kappa_{01}^2(\mu) \sim -(\mu - \mu_c)$, implying that when $\mu < \mu_c$, ε_{01} is positive and $\kappa_{01}(\mu) \sim \sqrt{\mu_c - \mu}$ is real and positive and that when $\mu > \mu_c$, ε_{01} is negative and $\kappa_{01}(\mu) \equiv i\kappa'_{01} \sim i\sqrt{\mu - \mu_c}$ is imaginary. The negative value of ε_{01} implies an instability towards a mixed spiral state. As Figure 4 illustrates, the zeros of Z_{ν_0} at higher values of κ (κ_{02}, κ_{11}, etc.) continue to exist, but their energies are much greater than that of ε_{01}.

3.3. Eigenfunctions and Expansion of the Frank Energy

Now, we proceed with our calculation of the normalized eigenfunctions. The solutions u_{mn} to Equation (10) are all linear in $Z_\nu(kr)$ with a normalization coefficient $V_{mn}^{-1/2}$ (with units of inverse length) such that

$$\int_{R_1}^{R_2} dr\, r\, u_{mn}(r) u_{mn'}(r) = \int_{R_1}^{R_2} dr\, r\, V_{mn}^{-1} Z_{\nu_m}^2(\kappa_{mn} r/R_1) = \delta_{nn'}\,, \tag{21}$$

which yields

$$V_{mn} = \left(\frac{R_2}{\kappa_{mn}}\right)^2 \gamma_{mn}\,, \tag{22}$$

where

$$\gamma_{mn} = \int_{\kappa_{mn}/\mu}^{\kappa_{mn}} dy\, y\, Z_{\nu_m}^2(y)\,, \tag{23}$$

is a dimensionless integral depending on κ_{mn} and the ratio of radii μ.

Figure 5 plots the radial eigenfunctions $u_{m1}(r)$ for our sample configuration with imaginary ν_0. It is noteworthy that the eigenfunction with the lowest energy, $u_{01}(r)$, is peaked near the defect core because its μ is close to μ_c. This is qualitatively different from the other sample configurations with real ν_m ($m > 0$) which are much less localized. Note that the curves in this figure are functions of r/R_1 at fixed μ. This means that peaks in the curve will have a definite value of $R_1 = R_2/\mu$ regardless of the value of R_2.

We now have all of the components to express f in terms of the solutions to the eigenvalue problem,

$$f(r,\phi) = \sum_{mn} A_{mn} \Psi_{mn}(r,\phi)\,, \tag{24}$$

with

$$\Psi_{mn}(r,\phi) = \frac{1}{\sqrt{2\pi}} u_{mn}(r)\, e^{im\phi}\,. \tag{25}$$

Note that the product eigenfunctions as a whole satisfy the orthonormality relations

$$\int dr d\phi\, \Psi_{mn}^*(r,\phi) \Psi_{m'n'}(r,\phi) = \delta_{mm'}\delta_{nn'}\,, \tag{26}$$

and that the expansion coefficients A_{mn} have units of the square root of an area. Finally, using Equation (24) and the orthnormality of the wavefunctions (Equation (26)), we expand the harmonic Frank energy in terms of the in the amplitudes A_{mn}:

$$F_h = \frac{1}{2}\sum_n A_{0n}^2 \varepsilon_{0n} + \sum_{m>0,n} |A_{mn}|^2 \varepsilon_{mn}\,. \tag{27}$$

4. Correlation Functions

Our goal in this section is to provide expressions for the full time-dependent f-correlation functions. A necessary first step is to define our dynamics. The real dynamics of the **c**-director is quite complicated with interactions between fluid flow and **c** and complicated anisotropic dissipative processes. Here, we will content ourselves with the simplest purely-dissipative dynamical model in which

$$\partial_t f(r,\phi) = -\Gamma \frac{\delta F}{\delta f(r,\phi)}\,, \tag{28}$$

where Γ, which we set equal to $10\frac{s}{Kg}$ for illustrative purposes in what follows, is a kinetic coefficient given by the inverse of the rotational viscosity γ_1 of the mesogens. Thus, the dynamical equation has the same functional derivative with respect to $f(\mathbf{r})$ as Equation (6), implying that the experimentally measured inverse decay times are necessarily given by $\Gamma\varepsilon_{mn}$:

$$\begin{aligned}\partial_t A_{0n} &= -\Gamma \frac{\partial F_h}{\partial A_{0n}} = -\Gamma\, \varepsilon_{0n} A_{0n}\,,\\ \partial_t A_{mn} &= -\Gamma \frac{\partial F_h}{\partial A^*_{mn}} = -\Gamma\, \varepsilon_{mn} A_{mn}\,.\end{aligned} \tag{29}$$

These equations of motion are readily integrated with the result

$$A_{mn}(t) = A_{mn}(0)\, e^{-\Gamma\, \varepsilon_{mn} t}\,, \tag{30}$$

for both $m = 0$ and $m > 0$. Then, using the the standard equilibrium statistical weight $\exp[-F_h/(k_B T)]$ with k_B the Boltzmann constant and T the temperature, we can calculate the static equilibrium averages,

$$\left\langle A^2_{0n} \right\rangle = \frac{k_B T}{\varepsilon_{0n}}\,, \qquad \text{and} \qquad \langle A^*_{mn} A_{mn} \rangle = \frac{k_B T}{\varepsilon_{mn}} \tag{31}$$

from which we obtain

$$\langle A^*_{mn}(t) A_{mn}(0) \rangle = k_B T\, G_{mn}(t) \tag{32}$$

for the A-A correlations, where

$$G_{mn}(t) = \frac{1}{\varepsilon_{mn}}\, e^{-\Gamma\, \varepsilon_{mn} t}\,. \tag{33}$$

We can now express the f-correlation function as

$$\begin{aligned} C(r,,r',\phi-\phi',t) &= \langle f(r,\phi,t) f(r',\phi',0) \rangle \\ &= S_0(r,r',t) + \sum_{m>0} \left[S_m(r,r',t) e^{im(\phi-\phi')} + S^*_m(r,r',t) e^{-im(\phi-\phi')} \right], \end{aligned} \tag{34}$$

where for all m

$$S_m(r,r',t) = \sum_n \frac{k_B T}{2\pi\, \varepsilon_{mn}} e^{-\Gamma \varepsilon_{mn} t}\, u_{mn}(r) u_{mn}(r') \approx \frac{k_B T}{2\pi\, \varepsilon_{m1}} e^{-\Gamma \varepsilon_{m1} t}\, u_{m1}(r) u_{m1}(r')\,. \tag{35}$$

Recall from Equations (21) and (22) that $u_{mn}(r)$ depends implicitly on κ_{mn}, μ, and R_2. Note that the net effect of the relaxation dynamics is to replace the inverse energies in the static correlation function stated in Equations (32) and (35) by the time-dependent G's. Note also that for $t \to 0$, our time-dependent correlation functions reduce to their static counterparts as they should. The function $C(r,\phi) = C(r,r,\phi,0)$ is plotted in Figure 7.

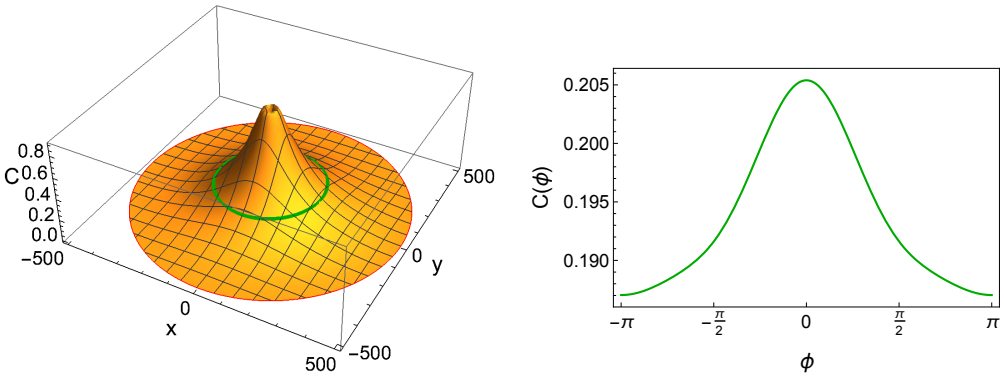

Figure 7. The correlation function $C(r,\phi) = C(r,r,\phi,0)$ defined in Equation (34). The left shows the correlation as a function of dimensionless coordinates in the plane. The green loop indicates an assumed probing radius of $r = R_{\text{Probe}}$. The right shows a zoom-in on the correlation function along the green loop.

5. Mixed Spiral States

In the absence of BCs, pure splay and bend states in an annular trap have respective energies $\pi K_s \ln \mu$ and $\pi K_b \ln \mu$ so that the splay state has lower energy when $K_s < K_b$ and the bend state lower energy when $K_b < K_s$. This simple reasoning changes when there are BCs, such as the perpendicular and tangential ones on both boundaries considered in this manuscript, because they enforce an alignment near the boundaries causing locally higher energy density than that of the uniform bulk configuration. Thus it is reasonable to ask whether the uniform splay configuration in an annular trap is the lowest energy state when $\beta = K_s/K_b > 1$, both when $\mu < \mu_c$ and when $\mu > \mu_c$. The fact that the energies of all modes, including ε_{01} remain positive for all $\mu < \mu_c$ establishes that the splay state is at least metastable and provides credible evidence that it is the true equilibrium state. The fact that ε_{01} is zero at $\mu = \mu_c$ also suggests that it is a precursor to a lower-energy mixed spiral state for $\mu > \mu_c$. To address these issues, we follow Refs. [31,32,34] and seek local extrema of the full Frank free energy of Equation (4). We first note that to find local extrema, it is useful to change variables to $x = \ln(r/R_1)$ and, for simplicity, to consider only $m = 0$ isotropic distortions so that f is independent of ϕ. The Frank energy expressed in terms of the x-variable is then

$$F_x = \pi K \int_0^{\ln \mu} dx[(1+\sigma\cos 2f)(\partial_x f)^2 + 2\sigma \sin 2f \partial_x f + (1-\sigma\cos 2f)]\,. \tag{36}$$

The second term in this expression is a perfect derivative and integrates to zero. Local extrema of F_x are then solutions to

$$\frac{\delta F_x}{\delta f(x)} = (1+\sigma\cos f)\frac{d^2 f}{dx^2} + \sigma \sin 2f \left(\frac{df}{dx}\right)^2 - \sigma \sin 2f = 0. \tag{37}$$

Solutions to this equation, other that of the pure splay for which $f = 0$, with perpendicular BCs will necessarily contain both splay and bend. We will refer to them as mixed states.

Our goal here is not an exhaustive analysis of the full phase diagram; rather it is to establish whether or not there are mixed states with lower energy than that of the pure splay state favored by BCs. To this end, we use the shooting method to find solutions to Equation (37) for the systems with homeotropic BCs. In our systematic, but not exhaustive calculations, we found no mixed states with lower energy than the the pure splay state when $\beta < 1$. But when $\beta > 1$, we find lower-energy mixed states for every $\mu > \mu_c$ we tested. Figure 8 plots the energy difference $\Delta F(\beta,\mu) = F - F_{\text{splay}}$ in units of πK_s between the mixed and the pure splay state as a function of μ for different values of $\beta > 1$. Curves for all β as calculated by the shooting technique are zero for $\mu < \mu_c$ and negative for $\mu > \mu_c$, establishing that the transition from the pure splay state to the mixed state is second order.

Figure 9 plots the profile of $f(r/R_1)$ for $\beta = 1.25$ and selected values of $\mu > 1$. It shows that the magnitude of f increases with increasing μ. It also shows a pronounced peak in f near the core, consistent with the observations of Ref. [34]. It is worth emphasizing again that the perpendicular boundary conditions guarantee that right at the two boundaries the defect is forced to have a splay configuration, but the configuration at any radius between R_1 and R_2 is mixed splay and bend.

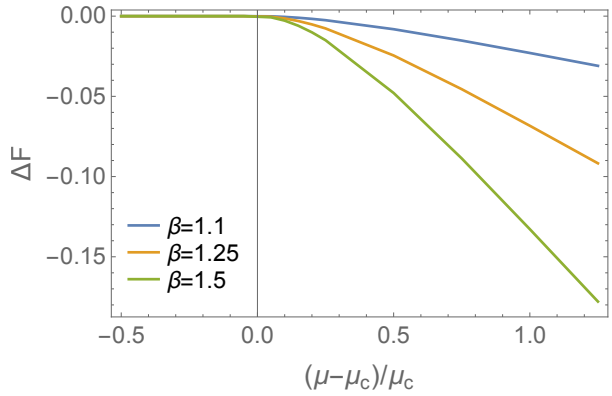

Figure 8. Plots of $\Delta F(\beta, \mu)$ calculated from Equation (37) as a function of $[\mu - \mu_c(\beta)]/\mu_c(\beta)$ for different values of β. Note, $\mu_c(x)$ grows exponentially as β approaches 1, and the regions depicted in this figure are relative to a large value of μ for small $\beta - 1$.

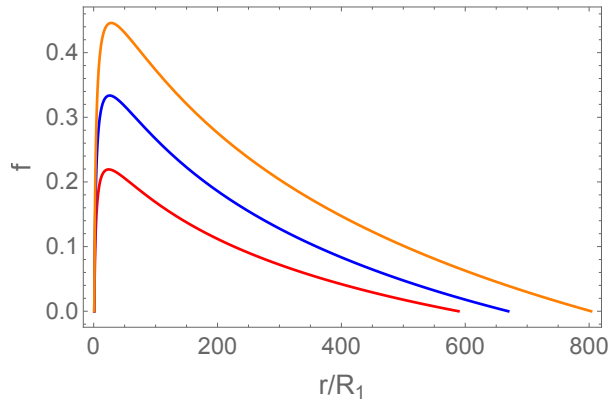

Figure 9. Plot of $f(r/R_1)$ for mixed states with $\beta = 1.25$ and for different values for μ: $\mu/\mu_c = 1.1$ (red), $\mu/\mu_c = 1.25$ (blue), and $\mu/\mu_c = 1.5$ (orange). Note the peak in amplitude near the core.

6. Two Calculational Procedures

Upon comparing Equations (4) and (36), it is natural to ask why not continue with the less complex Equation (36) to investigate the stability of the splay state. The answer is Equation (36) does not predict excitation energies and decay times that are described by the dynamical equation (Equation (28)) for the **c**-director and measured in standard experiments. To see how, we express $f(r, \phi)$ as a function, $f(x, \phi)$ of $x = \ln(r/R_1)$ rather than r:

$$f(x, \phi) = \sum_m f_m(x) e^{im\phi}, \tag{38}$$

where $f_m(x)$ is taken to be unitless. The harmonic energy of Equation (5) then becomes,

$$F_h^x = \frac{1}{2} \int_1^{\ln \mu} dx \int_0^{2\pi} d\phi \left[(K_b - K_s) f^2 + K_b (\partial_x f)^2 + K_s (\partial_\phi f)^2 \right], \tag{39}$$

Note the differences between Equations (5) and (39):

1. Equation (5) is integrated over $2D$ volume elements $rdrd\phi$ and Equation (39) over the $1D$ volume element dx.

2. Equation (5) has a factor of $1/r^2$ in front of the $[(K_b - K_s)f^2 + K_s(\partial_\phi f)^2]$ whereas that term is simply $[(K_b - K_s)f^2 + K_s(\partial_\phi f)^2]$ in Equation (39).
3. The change of variables from r to x changed the free energy from a $2D$ form to a form equivalent to a $1D$ one.

With the aid of $\delta f(x)/\delta f(x') = \delta(x - x')$, the new eigenvalue equation for the radial function $f_m(x)$ reflects these differences:

$$\frac{1}{\pi}\frac{\delta F_h^x}{\delta f_m(x)} = -K_b\left[\frac{d^2 f_m}{dx^2} + \Big(1 + \beta(m^2 - 1)\Big)f_m\right] = \bar{\epsilon}_m f_m. \tag{40}$$

The solution to this equation is

$$f_m(x) = \sin qx \tag{41}$$

where

$$q \to q_n = \frac{n\pi}{\ln \mu} \tag{42}$$

to satisfy the boundary conditions $f_m(0) = 0$ and $f_m(\ln \mu) = 0$. The resultant energy is

$$\bar{\epsilon}_{mn} = K_b[q_n^2 + 1 + \beta(m^2 - 1)]\,, \tag{43}$$

which is surely different from the energy functions calculated in Section 3.2: it has a different analytic form from that of ε in Equation (16) does, and it has units of energy rather than energy density. But $\bar{\epsilon}_{01} = 0$ defines the limit of stability, which is identical to Equation (18) obtained from $\varepsilon_{01} = 0$. Thus the two approaches produce the same critical line in the two-dimensional space of β and μ, but away from the critical line, their mode energies are different, even though they both reflect stability of the splay phase, as long as their respective energies are positive. Experimental measurements of fluctuations of the **c**-director are controlled by the dynamics of $\mathbf{c}(r, \phi, t)$, as described by Equation (28) which depends on $\delta F_h/\delta f(\mathbf{r})$ rather than $\delta F_h^x/\delta f_m(x)$. Thus, correlation function measured, for example, by video imaging, depend on ε_{mn} and not $\bar{\epsilon}_{mn}$.

7. Review and Discussion

In summary, we have analyzed fluctuations and phase behavior of splay and bend $+1$ disclination defects trapped in an annular region defined by the area between an outer circle of radius R_2 and a smaller concentric circle of radius R_1 with either perpendicular or tangential BCs at the two circular boundaries. If $\beta = K_s/K_b < 1$ under perpendicular BC's, the splay defect is stable for all values of $\mu = R_2/R_1$, where K_s and K_b are the 2D splay and bend Frank constants, respectively, but when $\beta > 1$, the defect is only stable for μ less than a critical value $\mu_c(\beta)$, Equation (18). At $\mu = \mu_c$, the defect undergoes a continuous (second-order) transition to a spiral state. Under tangential BCs, the behavior of the defect follows the same scenario as that of the splay state except with K_s and K_b interchanged, i.e., the bend defect is stable for all μ when $\beta^{-1} = K_b/K_s < 1$ and unstable to a mixed spiral defect when $\beta^{-1} > 1$ and $\mu > \mu_c(\beta^{-1})$. Our treatment includes analytical calculations of normal-mode energies, associated eigenfunctions, and related two-point director correlation functions relative to the pure splay and bend states. We point out the differences between our approach, which calculates properties that are observable in real experiments, and an approach used to identify critical points and to calculate spiral configurations. The two approaches predict the same critical points and mixed configurations and their domain of stability. They do, however, predict different values for normal-mode energies and their wave functions except at phase boundaries.

We have not found any published papers reporting experimental measurements of fluctuations of trapped defects in smectic-C films or other media. It does seem, however, that video imaging, for example, of fluctuations in the cloverleaf pattern produced by "pure" bend or splay configurations should be possible. In addition, the existence of materials

covering a wide range of β's (for example by mixing mesogens [33–35] with different Frank constants, chirality, or polarity) and the possibility of modifying the properties of the inner circles with different inclusions [18,32] (e.g., dust particles or different fluids) suggests an interesting avenues for future research. Measurements of fluctuations about 3*D* hedgehogs trapped in micron-scale emulsion droplets with nanoscale water droplets at their center have been carried out successfully [38], and their results are well explained by the 3*D* version [39] of the theory presented here.

Author Contributions: Conceptualization: O.S. and T.C.L.; Methodology: O.S. and T.C.L.; Writing—original draft: O.S.; Writing—review & editing: O.S. and T.C.L.; Supervision: T.C.L.; Funding acquisition: T.C.L. All authors have read and agreed to the published version of the manuscript.

Funding: This work was supported by US National Science Foundation Penn MRSEC under Grant No. DMR17-20530.

Data Availability Statement: Not applicable.

Conflicts of Interest: Neither author has any conflict of interest.

References

1. Chen, X.; Korblova, E.; Dong, D.P.; Wei, X.Y.; Shao, R.F.; Radzihovsky, L.; Maclennan, M.A.; Bedrov, D.; Walba, D.M.; Clark, N.A. First -principles experimental demonstration of ferroelectricity in a thermotropic nematic liquid crystal: Polar domains and striking electro-optics. *Proc. Natl. Acad. Sci. USA* **2020**, *117*, 14021–14031. [CrossRef] [PubMed]
2. Bohley, C.; Stannarius, R. Inclusions in free standing smectic liquid crystal films. *Soft Matter* **2008**, *4*, 683–702. doi: 10.1039/b715124a. [CrossRef]
3. Harth, K.; Stannarius, R. Topological Point Defects of Liquid Crystals in Quasi-Two-Dimensional Geometries. *Front. Phys.* **2020**, *8*, 112. [CrossRef]
4. Young, C.Y.; Pindak, R.; Clark, N.A.; Meyer, R.B. Light-scattering study of two-dimensional molecular-orientation in a freely suspended ferroelectric liquid-crystal film. *Phys. Rev. Lett.* **1978**, *40*, 773. [CrossRef]
5. Rosenblatt, C.S.; Pindak, R.; Clark, N.A.; Meyer, R.B. Freely Suspended Ferroelectric Liquid-Crystal Films—Absolute Measurements of Polarization, Elastic Constant, and Viscosities. *Phys. Rev. Lett.* **1979**, *42*, 1220. [CrossRef]
6. Rosenblatt, C.S.; Pindak, R.B.M.R.; Clark, N.A. Temperature Behavior of Ferrolelectric Liquid-Crystal Thin-Films—Classical XY-System. *Phys. Rev. A* **1980**, *21*, 140. [CrossRef]
7. Pindak, R.; Young, C.Y.; Meyer, R.B.; Clark, N.A. Macroscopic Orientation Patterns in Smectic-C Films. *Phys. Rev. Lett.* **1980**, *45*, 1193–1196. [CrossRef]
8. Winkle, D.H.V.; Clark, N.A. Direct Measurement of Orientation Correlations—Observation of the Landau-Peierls Divergence in a Freely Suspended Tilted Smectic Film. *Phys. Rev. Lett.* **1984**, *53*, 1157–1160. [CrossRef]
9. Winkle, D.H.V.; Clark, N.A. Direct Measurement of Orientation Correlations in a Two-Dimensional Liquid-Crystal System. *Phys. Rev. A* **1988**, *38*, 1573–1589. [CrossRef]
10. Van Winkle, D.H.; Dierker, S.B.; Clark, N.A. Raman-Scattering from Freely Suspended Liquid-Crystal Films. *J. Chem. Phys.* **1989**, *91*, 5212–5217. [CrossRef]
11. Muzny, C.D.; Clark, N.A. Direct Observation of the Brownian-Motion of a Liquid-Crystal topological Defect. *Phys. Rev. Lett.* **1992**, *68*, 804–807. [CrossRef] [PubMed]
12. Maclennan, J.E.; Sohling, U.; Clark, N.A.; Seul, M. Textures in Hexatic Films of Nonchiral Liquid-crystals–Symmetry-Breaking and Modulated Phases. *Phys. Rev. E* **1994**, *49*, 3207–3224. [CrossRef]
13. Link, D.R.; Radzihovsky, L.; Natale, G.; Maclennan, J.E.; Clark, N.A.; Walsh, M.; Keast, S.S.; Neubert, M.E. Ring-pattern dynamics in smectic-C* and smectic-C-A* freely suspended liquid crystal films. *Phys. Rev. Lett.* **2000**, *84*, 5772–5775. [CrossRef] [PubMed]
14. Pattanaporkratana, A.; Park, C.S.; Maclennan, J.E.; Clark, N.A. Manipulation of disk-shaped islands on freely suspended smectic films and bubbles using optical tweezers. *Ferroelectrics* **2004**, *310*, 275. [CrossRef]
15. Chao, C.Y.; Lo, C.R.; Liu, Y.H.; Link, D.R.; Maclennan, J.E.; Clark, N.A.; Veum, M.; Huang, C.C.; Ho, J.T. Unusual thickness-dependent thermal behavior in chiral smectic free-standing liquid-crystal films. *Mol. Cryst. Liq. Cryst.* **2004**, *412*, 2003–2010. [CrossRef]
16. Link, D.R.; Chattham, N.; Maclennan, J.E.; Clark, N.A. Effect of high spontaneous polarization on defect structures and orientational dynamics of tilted chiral smectic freely suspended films. *Phys. Rev. E* **2005**, *71*, 021704. [CrossRef] [PubMed]
17. Pattanaporkratana, A.; Park, C.S.; Maclennan, J.E.; Clark, N.A. Direct measurement of interaction forces between islands on freely suspended smectic C films using multiple optical tweezers. *Ferroelectrics* **2006**, *344*, 314–324. [CrossRef]
18. Silvestre, N.M.; Patricio, P.; da Gama, M.M.T.; Pattanaporkratana, A.; Park, C.S.; Maclennan, J.E.; Clark, N.A. Modeling dipolar and quadrupolar defect Structures generated by chiral islands in freely suspended liquid crystal films. *Phys. Ref. E* **2009**, *80*, 041708. [CrossRef]

19. Eremin, A.; Baumgarten, S.; Harth, K.; Stannarius, R.; Nguyen, Z.H.; Goldfain, A.; Park, C.S.; Maclennan, J.E.; Glaser, M.A.; Clark, N.A. Two-Dimensional Microrheology of Freely Suspended Liquid Crystal Films. *Phys. Rev. Lett.* **2011**, *107*, 268301. [CrossRef] [PubMed]
20. Kuriabova, T.; Powers, T.R.; Qi, Z.Y.; Goldfain, A.; Park, C.S.; Glaser, M.A.; Maclennan, J.E.; Clark, N.A. Hydrodynamic interactions in freely suspended liquid crystal films. *Phys. Rev. E* **2016**, *94*, 052701. [CrossRef]
21. Radzihovsky, S.P.; Cranfill, C.; Nguyen, Z.; Park, C.S.; Maclennan, J.E.; Glaser, M.A.; Clark, N.A. Two-dimensional island emulsions in ultrathin, freely-suspended smectic liquid crystal films. *Soft Matter* **2017**, *13*, 6314–6321. [CrossRef] [PubMed]
22. Yoon, D.K.; Zhu, C.; Kim, Y.H.; Shen, Y.Q.; Jung, H.T.; Clark, N.A. Dendritic growth in a two-dimensional smectic E freely suspended film. *Mol. Sys. Des. Eng.* **2020**, *5*, 815–819. [CrossRef]
23. Chattham, N.; Zhu, C.; Cheng, X.; Limtrakul, J.; Tschierske, C.; Maclennan, J.E.; Clark, N.A. Direct observation of two-dimensional nematic and smectic ordering in freely suspended films of a bolaamphiphilic liquid crystal. *Soft Matter* **2011**, *7*, 9978–9982. [CrossRef]
24. Mermin, N.D. Topological Theory in Ordered Media. *Rev. Mod. Phys.* **1979**, *51*, 591–648. [CrossRef]
25. Brinkman, W.F.; Cladis, P.E. Defects in Liquid Crystals. *Phys. Today* **1982**, *35*, 48–54. [CrossRef]
26. Chandrasekhar, S.; Ranganath, G.S. The structure and energetics of defects in liquid crystals. *Adv. Phys.* **1986**, *35*, 507–596. [CrossRef]
27. de Gennes, P.G.; Prost, J. *The Physics of Liquid Crystals*, 2nd ed.; Oxford University Press: London, UK, 1995; Chapters 4 and 9.
28. Chaikin, P.M.; Lubensky, T.C. *Principles of Condensed Matter Physics*; Cambridge Press: Cambridge, UK, 1995; Chapter 9.
29. Loft, R.; DeGrand, T.A. Numerical simulation of dynamics in the xy-model. *Phys. Rev. B* **1987**, *35*, 8528–8541. [CrossRef]
30. Pleiner, H. Dynamics of disclination point in smectic-C and smectic-D* liquid-crystal films. *Phys. Rev. A* **1988**, *37*, 3986–3992. [CrossRef] [PubMed]
31. Loh, K.-K.; Kraus, I.; Meyer, R.B. Chiral hedgehog textures in two-dimensional XY-like ordered domains. *Phys. Rev. E* **2000**, *62*, 5115. [CrossRef] [PubMed]
32. Lee, J.-B.; Konovalov, D.; Meyer, R. Textural Transformations in islands on free standing Sm-C^* films. *Phys. Rev. E* **2006**, *73*, 051705. [CrossRef]
33. Dolganov, P.V.; Dolganov, V.K.; Cluzeau, P. The effect of spontaneous polarization on two-dimensional elasticity of smectic liquid crystals. *JETP* **2013**, *116*, 1043–1049. [CrossRef]
34. Dolganov, P.V.; Cluzeau, P. Manifold configurations of the director field formed by topological defects in free and confined geometry in smectic films. *Phys. Rev. E* **2014**, *90*, 062501. [CrossRef] [PubMed]
35. Dolganov, P.V.; Shuravin, N.S.; Dolganov, V.K.; Kats, E.I. Topological defects in smectic islands in freely suspended films. *JETP Lett.* **2015**, *101*, 453–458. [CrossRef]
36. Lee, J.; Pelcovits, R.A.; Meyer, R.B. Role of electrostatics in the texture of islands in free-standing ferroelectric liquid crystal films. *Phys. Rev. E* **2007**, *75*, 051701. [CrossRef] [PubMed]
37. Link, D.R.; Natale, G.; Clark, N.A.; Maclennan, J.E.; Walsh, M.; Keast, S.S.; Neubert, M.E. Anticlinic Smectic-*C* Surfaces on Smectic-*A* Freely Suspended Liquid-Crystal Films. *Phys. Rev. Lett.* **1999**, *82*, 2508. [CrossRef]
38. de la Cotte, A.; Stenull, O.; Ettinger, S.; Collings, P.J.; Lubensky, T.C.; Yodh, A.G. Giant Director Fluctuations in Liquid Crystals Droplets. *Phys. Rev. E Submitted*.
39. Stenull, O.; Ettinger, S.; Cotte, A.d.; Collings, P.J.; Yodh, A.G.; Lubensky, T.C. *Submitted to Phys. Rev. E*.